Published in final edited form as:
Acta Biomater. 2008 July ; 4(4): 783–790. doi:10.1016/j.actbio.2008.02.010.

Non-invasive monitoring of tissue scaffold degradation using ultrasound elasticity imaging

Kang Kim[*], **Claire G. Jeong**, and **Scott J. Hollister**
Department of Biomedical Engineering, University of Michigan, Ann Arbor, MI 48109, USA

Abstract

Non-invasively monitoring the extent of cell growth, scaffold degradation and tissue development will greatly help tissue engineers to monitor in vivo regenerate tissue function and scaffold degradation. Currently available methods for tissue and scaffold degradation analysis, such as histology and direct mechanical measurements, are not suitable for continuous monitoring of the same sample in vivo as they destroy cells, tissue matrix and scaffolds. In addition, different samples are prepared and measured at varying times, but high tissue growth deviation between specimens and the need for monitoring tissue growth and scaffold degradation at different times requires large sample numbers for statistical analysis. Ultrasound elasticity imaging (UEI) based on phase-sensitive speckle tracking can characterize the internal structural, compositional and functional change of biomaterial scaffolds and engineered tissues at high resolution. In this study, UEI resolution was 250 lm (axial) by 500 μm (lateral) using a commercial ultrasound transducer centered at 5 MHz. This method allows characterization of both globally and locally altered scaffold and engineered tissue elastic properties. Preliminary in vitro and in vivo results with poly(1,8-octanediol-co-citrate) scaffolds support the feasibility of UEI as a non-invasive quantitative monitoring tool for scaffold degradation and engineered tissue formation. This novel non-invasive monitoring tool will provide direct, time-dependent feedback on scaffold degradation and tissue ingrowth for tissue engineers to improve the design process.

Keywords

Non-invasive imaging; Strain imaging; Tissue scaffold degradation; Tissue scaffold mechanical property; Ultrasound elasticity imaging

1. Introduction

In tissue engineering, biodegradable polymer scaffolds are used to deliver cells and regenerate tissue as well as provide temporary mechanical support. There are two main challenges in creating the ideal biodegradable polymer scaffold: (i) the scaffold must have a defined shape and porous internal architecture suitable to direct tissue ingrowth with appropriate mechanical and degradation properties; and (ii) the scaffold must have appropriate surface properties to provide favorable conditions for cells to attach, proliferate, differentiate and produce extracellular matrix [1]. The success of aliphatic polyesters in tissue engineering relies largely on their degradability and biocompatibility, as well as on their mechanical properties. In principle, the degradation rate of the scaffold should match

---

[*] Corresponding author. Tel.: +1 734 763 5448; fax: +1 734 936 1905. kangkim@umich.edu (K. Kim)..

the rate of tissue formation, hence the degradation behavior of a scaffold has a critical impact on the long-term performance of a tissue-engineered cell/scaffold construct in vivo.

Therefore, non-invasively monitoring the extent of scaffold degradation and tissue development will greatly help tissue engineers better evaluate regenerative therapies. It would also be valuable to measure matrix development, such as collagen, elastin and hard tissues, which could determine the load-bearing capability of the scaffold/tissue construct. To optimize therapies, it is highly desirable to understand relative rates of tissue regeneration and scaffold degradation for the same specimen as a function of time. Currently, available analysis methods for quantifying tissue formation are histology and direct mechanical measurements. Even though these methods provide good images for cell phenotype and proliferation, and mechanical characterization such as compressive moduli of scaffolds, they require animal sacrifice and scaffolds destruction, hence samples cannot be reused after characterization. In addition, different samples are prepared and measured at varying times, but high tissue growth deviation between specimens requires large sample numbers for statistical analysis. Ideally, tissue engineers need a system that can non-invasively monitor tissue growth and consequent scaffold degradation in the same specimen over time. Other imaging methods, such as magnetic resonance imaging and computed tomography (CT), provide internal scaffold structural information, but they are limited to providing only morphological information, and scanning and image reconstruction procedures are quite extensive [2].

Ultrasound elasticity imaging (UEI) has been found to be a valuable non-invasive tool to investigate mechanical characteristics of biological tissue [3–6]. It estimates tissue motion based on speckle tracking between two frames before and after deformation of the tissue. In UEI the excitation is produced by actually pushing on tissue with an ultrasound transducer itself and recording the tissue deformation with real-time ultrasound images [4,7]. This constitutes a near static deformation with an external force. Combinations of static or dynamic deformations with internal or external surface forces to induce deformations have also been explored [8,9]. Speckle tracking was initially introduced in one dimension (1-D) to estimate tissue motion along the axial direction (the beam propagation direction) [4,10] and has been expanded into 2-D. 2-D speckle tracking measures displacements of the speckles in both axial and lateral (perpendicular to the beam direction in the imaging plane) directions [11–15]. The most commonly used elasticity imaging techniques are based on 2-D correlation-based speckle tracking methods [12–15]. Speckle displacements are estimated from correlation lags corresponding to the maximum correlation coefficient between the frames. In the past decade, elasticity imaging based on speckle tracking has been shown to have great potential for clinical use [3,4,7,16–20], where several groups have also explored high spatial resolution ultrasound speckle tracking systems for intravascular applications [18,21–23]. UEI using transcutaneous linear probes has also been successfully applied to other in vivo applications, including, thrombus aging/maturational evaluation in human lower limb deep venous thrombosis [24,25], breast cancer diagnosis [26,27], differentiation of benign and malignant thyroid masses [28], differentiation of benign and malignant cervical lymph nodes [29], prostate cancer detection [30,31], renal transplant graft nephropathy evaluation [32], characterization of arterial wall stiffness for early atherosclerosis diagnosis [8,33], assessment of myocardial wall stiffness for detection of contractile dysfunction [34] and atheromata assessment for determining vulnerable plaque [35,36].

UEI combines two procedures: (i) the application of controlled deformation to the study object; and (ii) phase-sensitive, 2-D ultrasound speckle tracking and evaluation of internal tissue motion, i.e. measurement of displacement and strain components. UEI will provide full internal mechanical and structural characteristics of the biomaterial tissue scaffold and engineered tissue as a measure of the scaffold degradation and tissue regeneration process. In this paper, the feasibility of UEI is demonstrated by applying this technique to monitor the in vitro and in vivo degradation processes of poly(1,8-octanediol-co-citrate) (POC) scaffolds.

POC is a strong, elastomeric, biodegradable, hydrophilic "cell-friendly" material which shows promise for soft tissue engineering. Furthermore, it has the following advantages: non-toxic monomers, a relatively simple synthesis without addition of catalysts or cross-linking reagents, cost-effective scale-up, controllable mechanical and biodegradation properties and easy processing, and inherent surface affinity for various cell types including chondrocytes and bone marrow stromal cells. Recently, Yang et al. have shown that POC has properties favorable for cartilage matrix regeneration [37]. POC is synthesized by reacting the polyfunctional monomer citric acid with the difunctional monomer 1,8-octanediol to create a polyester network with a controllable number of crosslinks to tailor the elasticity and biodegradability of the resulting material.

POC is degraded by hydrolysis of its ester linkages in physiological conditions and its byproducts, citric acid and 1,8-octanediol, are excreted by the body. Citric acid is a non-toxic metabolic product of the Krebs cycle in the body and 1,8-octanediol enables ester bonds to form with citric acid and is water-soluble with no reported toxicity. These monomers ensure a beneficial property of the degradation process leaving no insoluble or toxic complexes in the body. One of the unique properties of POC is that its mechanical properties can easily be tailored by changing curing temperature and time, monomer molar ratio, and the presence of vacuum when curing. Even though Kang et al. [38] have shown POC degradation profiles in vitro using phosphate buffered solution (PBS) at 37 °C, the degradation behavior in vivo has not been elucidated. Since POC is known as a relatively fast-degradable polymer, careful monitoring of mechanical property changes due to degradation behavior will be required to relate to tissue formation.

In this study, we focus on showing the feasibility of noninvasive monitoring of scaffold degradation using UEI by comparing UEI measures with standard mechanical testing and weight measures of degradation. UEI is applied in vitro to POC scaffolds embedded in a gelatin phantom. In vivo UEI on POC scaffolds implanted subcutaneously in a mouse is also performed to investigate the feasibility of this technique as a non-invasive monitoring tool of scaffold degradation.

2. Materials and methods

2.1. Scaffold design

Previously developed image-based design processes and software were used to design POC scaffold architecture [39–41]. In image-based design, 3-D topology is represented as densities from 0 to 255 in a structured voxel data-set. Thresholding the voxel data into materials and void gives the final topology. To design scaffolds with hierarchical features, image databases are developed for each scale of structure. For the cartilage scaffolds in this study, the cubical pore architectures designed at the 0.1–1 mm scale were generated using software written in the program Interactive Data Language (IDL, ITT Industries, Inc. Boulder, CO). Scaffold external shape for mechanical testing and subcutaneous implantation was also generated using specially written IDL programs. Finally, these two scale levels of databases were merged using Boolean operations to define the final image-based scaffold design. For this study, we used a 3-D cylindrical shaped scaffold with cubical pore shapes where the final 3-D architecture is created by first designing a unit mathematical cell [39] and repeating this cell periodically in 3-D space.

2.2. POC scaffold fabrication

Poly(1,8-octanediol-co-citrate) pre-polymer (pPOC) was synthesized following protocols described by Ameer and colleagues [37,38] with some modification. Briefly, an equi-molar ratio of 1,8-octanediol and citric acid was reacted at 162.5 °C (160–165 °C) for 15 min with gentle stirring and a constant flow of N_2 into the system. Then the system temperature was subsequently lowered to 140 °C and the mixture stirred for another 30–45 min to react further. Post-polymerization of the pre-polymer was done through a modified protocol in order to fabricate designed architecture scaffolds using solid freeform (SFF) fabrication methods. Before post-polymerization of the pre-polymer into architecture scaffolds, wax molds with architecture were built by a Solidscape Patternmaster™ machine. Then hydroxyapatite (HA) molds (inverse of the wax molds) were fabricated using thermally curable HA slurry poured into the wax molds. The pre-polymer was poured into PTFE molds and pre-prepared inverse HA molds were embedded within the pPOC. The pPOC/HA construct inside the PTFE mold was post-polymerized at 80 °C for 4 days without vacuum in an oven. The HA + POC construct was removed from the PTFE mold and the HA mold was then dissolved from the construct using an acid solvent, RDO (APEX Engineering Products Corp., Plainfield, IL) to obtain the final POC scaffold. The fabrication procedure is illustrated in Fig. 1.

2.3. In vitro scaffold degradation

In vitro and in vivo scaffold degradation was evaluated using both conventional methods and a novel ultrasound imaging technique. The weight loss (%) vs. degradation time and compressive modulus vs. degradation time were plotted to obtain the correlation between compressive modulus vs. weight loss (%). The pH of the degradation medium in every test tube was measured with a pH meter before and at every week interval of the scaffold degradation.

The dry scaffolds were immersed in medium (high glucose DMEM + 10% fetal bovine serum (FBS) + 1% P/S, Gibco) at 37 °C and shaken by an orbital shaker to reach desired degradation 45% faster and recovered at different periods of time, up to 14 days. After scaffold recovery, the water on the surface was gently removed by filter paper. Then samples for each time point were weighed after water removal and subsequently dried in vacuum until a constant weight was obtained. The weight of the dry scaffold was measured (W_t) and compared with its original weight (W_0). The weight lost by degradation was determined as: weight loss = $[(W_0\ W_t)/W_0] \times 100\%$. The initial porosity of each scaffold before degradation was measured by using μCT and the dimension of each scaffold was measured by a caliper to keep the original dimension and to avoid any abnormal dimensional changes due to swelling.

2.4. Phantom preparation

For in vitro UEI, three scaffolds were embedded 30 mm apart in a phantom of 1% gelatin (G-2500, Sigma Aldrich Corp., St. Louis, MO) mixed with 0.5% ultrasound scatterer (polystyrene spheres, Amberlite, Sigma Chemical Co., MO). The scaffolds were soaked in deionized water before being embedded in the gel phantom to avoid bubbles being trapped in the pores. A portion of the prepared gelatin solution was first poured into a cubic mould. The scaffold was then embedded halfway as soon as the gelatin starts form. The rest of the gelatin solution was immediately added to fill up the mould. After ultrasound imaging was performed at each stage of the degradation, the samples were recovered and returned to the subsequent degradation process.

2.5. In vitro UEI

A commercial ultrasound (US) scanner (iU22, Philips, Bothell, WA) was used to image and collect consecutive radiofrequency (RF) imaging frames in real-time at 49 Hz over 6 s during continuous deformation of the POC embedded gel phantom by a linear array ultrasound transducer (L8-4, centered at 5 MHz, Philips, Bothell, WA) (see Fig. 2). The ultrasound transducer was fixed to a laboratory designed deformation device to induce a uniform and consistent average strain. The transducer surface measures around 50 mm by 16 mm and directly compresses the gelatin phantom. A phase-sensitive correlation-based 2-D speckle tracking algorithm was applied to determine the in-plane frame-to-frame displacement [15]. To improve the signal-to-noise ratio, frame decimation by factor of 5–10 was applied and incremental frame-to-frame displacements were accumulated referenced to the original geometry (Lagrangian presentation). The axial normal strain was calculated by taking a spatial derivative of the accumulated displacements in the axial direction (ultrasound beam and externally applied deformation direction). Strains for the scaffold at different degradation stages were normalized to the magnitude of the average strain (about 5–10% at total) estimated from the phantom thickness change observed by the ultrasound reflection from the bottom of the phantom, to ensure standardized strain measurements. The speckle in ultrasound image measured about 210 μm (axial) by 380 μm (lateral). The kernel size of the speckle tracking, which will determine the imaging resolution, was set to be 250 μm (axial) by 500 μm (lateral) in this study, which is about 1.2 times the speckle size [15]. The average normalized strain inside the scaffold was estimated to measure the overall alteration of the mechanical property. To examine the spatial variation of the structural degradation inside the scaffold, the coefficient of variation (COV = standard deviation/mean) of the normalized strain was also estimated [42].

2.6. Animal preparation and scaffold implantation

Three scaffolds were implanted subcutaneously in a 5-week-old immunocompromised NIH-III mouse under protocol approved by the University of Michigan Committee on the Use and Care of Animals. The animal was anesthetized with intramuscular injections of ketamine (50 μg g^{-1}) and xylazine (5 μg g^{-1}) in saline. Three dorsal subcutaneous pockets were created by blunt dissection and one scaffold was placed in each pouch. The scaffolds were positioned upright along the long axis of the cylinder. The implantation sites were closed with surgical wound clips. The animal was housed in group with free access to food and water.

2.7. In vivo UEI

Under the approved animal use protocol, the same RF data capturing procedure using the same US scanner as in the in vitro experiment described above was performed. The anesthetized mouse was placed on a custom-built platform in a prone position with its back exposed to the transducer. The imaging transducer also served to compress the scaffolds under the mouse's back surface and underlying tissue. The ultrasound transducer was fixed to a laboratory designed deformation device to induce a uniform and consistent average strain (Fig. 2). The RF frames were captured at a rate of 49 Hz while approximately 5–10% average strain was being generated over 6 s. The signal processing procedures and parameters are mostly same as those used in vitro. Strains for the scaffold at different degradation stages were normalized to the magnitude of the average strain (about 5–10% at total) estimated from the thickness change observed by the ultrasound reflection from the back of the mouse, to ensure standardized strain measurements. Note that 10% deformation corresponds to only 2 mm change out of 20 mm in abdomen thickness of the mouse.

2.8. Direct mechanical measurement

A mechanical measurement system developed in the laboratory capable of measuring the elastic modulus of small tissue samples was used [43]. It tolerates the constraints of biological tissue, such as limited sample size (≤1.5 cm^3) and imperfections in sample geometry. The pressing stamp is a cylinder with a diameter of 35 mm. The scaffolds after UEI on each stage of degradation were placed in the sample holder. The elastic modulus was determined by way of strain and simultaneous measurement of resulting force under conditions of continuous deformation.

3. Results

3.1. In vitro

As described above, six porous POC scaffolds (6.0 mm diameter, 4.0 mm height, 750 μm × 750 μm interconnected cubical pores, porosity 50%) were fabricated and tested. Three of the scaffolds were used for the in vitro study and the other three were implanted in the mouse for in vivo study. In the in vitro study, the scaffolds remained in medium for 14 days until they degraded up to an average 43% by weight loss. The weight measurements of each sample before and after the degradation are listed in Table 1. The accumulated strains referenced to the original geometry were imaged along with the B-scans (Fig. 3). The strain maps overlaid on top of the B-scans (second and third lows in Fig. 3) clearly indicated the degree of scaffold degradation. The average normalized strain generated inside of the scaffold after the degradation (–2.97 ± 0.74) of about 43% by weight was much higher than before the degradation (–0.43 ± 0.03) of the scaffolds. Note that a normalized strain of –1.0 represents that the region of the interest generates the same strain as the average strain estimated by the thickness change of the entire gelatin phantom. The average normalized strains on each sample are listed in Table 1. The increased normalized average strain reflects the weight loss and subsequent elastic property alteration. It was also observed that the strain maps become more inhomogeneous along with scaffold degradation (third row in Fig. 3). The COV after the degradation (25%) was much higher than before the degradation (7%). The increased inhomogeneity of the strain map reflects the possible heterogeneous distribution of structural degradation.

Based on the direct stress–strain measurement curve (Fig. 4), the elastic modulus was determined by taking the slope of the linear least squares fit on the original measurement curve. To assure consistent contact between the pressing stamp and the scaffold samples at the onset of deformations, measurement points were considered invalid if their associated force was less than 10% of the maximal pressing force. Those points with the natural strain greater than 30% were also discarded from elastic modulus estimation due to high deformation of the scaffold samples. The exclusion of the data points beyond this strain range may bias the elastic modulus estimates, but the bias does not alter the separation between before and after the degradation. Within this range of stress–strain relationship, first-order polynomial (linear) fit was applied to estimate the slope. All fits attained a high correlation ($r^2 > 0.95$; see Table 1). The mean elastic modulus among three samples before degradation was 74.1 ± 15.5 kPa. After 43% degradation by weight, the elastic modulus was reduced to 37.7 ± 5.5 kPa.

3.2. In vivo

After 7 days of implantation the weight of the scaffolds was reduced by 23% on average. The weight measurements of each sample before and after the degradation are listed in Table 1. The accumulated strains referenced to the original geometry were imaged along with the B-scans in Fig. 5. The strain maps overlaid on top of the B-scans reflects the degree of the scaffold degradation. Scaffolds after 23% weight degradation showed much higher strains (–1.40 ± 0.24) than those before degradation (–0.21 ± 0.01). The average normalized strains on each sample are listed in Table 1. The increase of inhomogeneity in the strain map was also observed along with the progression of the degradation, reflecting the spatial variation of the structural degradation inside the scaffolds. The COV before the degradation (4.8%) was increased to 17% after the degradation.

Based on the direct stress–strain measurement curve (Fig. 6), the elastic modulus was demonstrated in the same way as the in vitro data. The mean elastic modulus among three samples before degradation was 55.3 ± 1.4 kPa. After 23% degradation by weight, the elastic modulus was reduced to be 37.6 ± 3.9 kPa.

4. Discussion

In the in vitro experiments, the scaffolds after degradation exhibited much higher average strain than before degradation. This higher average strain directly reflects the overall alteration of the elasticity of the scaffold samples commensurate with the degradation. The percentage variation of the average normalized strains among the samples was relatively small, as low as 17%. The spatial distribution of the strain map in the scaffolds became inhomogeneous with degradation. The inhomogeneous strain patterns were different from one sample to the other. This could be due either to the random degradation process inside the scaffold structure or a different imaging cross section from one scaffold sample to the other. This inhomogeneity can also be a good signature of the degradation characteristics. This supports the feasibility of monitoring the distribution of the internal tissue ingrowth. The resolution of the strain maps presented in Figs. 3 and 5 is about the kernel size of the speckle tracking centered at 5 MHz, which is 250 μm in axial direction and 500 μm in lateral direction. With higher resolution, using higher frequency transducers up to 100 MHz, the internal structural degradation and tissue growth distribution can be imaged at a resolution down to tens of microns [44].

The in vivo elasticity imaging illustrates the same pattern of strain increase as found in the in vitro experiments of scaffold degradation. In this feasibility study of UEI for scaffold degradation, it was not intended to monitor tissue regeneration. Thus, the implantation period was limited to 7 days. At the end of the 7 days, a very small amount of granulation tissue was found attached to the surface of the scaffold and it was carefully rinsed off using regular PBS solution and drying off the PBS by filter paper before measuring the weight loss. For the same reasons as discussed for in vitro experiments, different samples show different inhomogeneous strain patterns in the in vivo experiment.

In summary, the strain in the scaffold increased after degradation both in vitro and in vivo. More experiments with a large number of scaffolds with different material and structural characteristics, such as different porosity, will be carried out to further verify results from this initial study. The average strain map clearly differentiates the scaffold before and after degradation both in vitro and in vivo. The increased inhomogeneity in the strain map also reflects the local variability of internal structural decomposition of the scaffold. Preliminary in vitro and in vivo results demonstrate the feasibility of non-invasive ultrasound elasticity imaging to characterize the inter-structural change of the tissue scaffold at high precision and resolution.

From the direct mechanical measurements, stress–strain curves (Figs. 4 and 6) also illustrate non-linear elastic behavior of the scaffold. Investigation on non-linearity and elastic modulus reconstruction will add important parameters to fully assess structural, compositional and functional characteristics of the scaffold and engineered tissue.

Depending on the individual pore shape and the distribution of the pores, the internal supporting structure may not be homogeneous inside the scaffold. The degradation process also may vary in space due to the different boundary conditions. To fully characterize the internal structural degradation process, 3-D elasticity imaging is also under investigation [45]. Using either a 2-D transducer array or the same 1-D linear probe used in this 2-D elasticity imaging, scanning the scaffold along the elevation direction (orthogonal to the 2-D imaging plane) using a translational stage at each step of deformation will provide a full 3-D strain map. For a uniform boundary condition, a deformation plate with a large surface area may need to be considered. Based on the 3-D displacement information, a 3-D elastic modulus reconstruction is also under development [46,47].

This technique can also be relatively easily integrated into a commercial ultrasound scanner for various animal studies and possibly translated into human clinical imaging tools.

5. Conclusion

Although limited by the number of samples and data points, the feasibility of ultrasound elasticity imaging as a non-invasive monitoring tool for the mechanical and degradation property of the tissue scaffolds was demonstrated in vitro and in vivo.

Acknowledgments

This work was supported in part by NIH grants DE-016129, HL-67647, HL-68658, HL-082640 and EB-003451. The authors thank Philips Ultrasound, Bothell, USA for their system support.

References

1. Gao J, Crapo PM, Wang Y. Macroporous elastomeric scaffolds with extensive micropores for soft tissue engineering. Tissue Eng 2006;12:917–25. [PubMed: 16674303]
2. Sun W, Darling A, Starly B, Nam J. Computer-aided tissue engineering: overview, scope and challenges. Biotechnol Appl Biochem 2004;39:29–47. [PubMed: 14563211]
3. Lerner RM, Parker KJ, Holen J, Gramiak R, Waag RC. Sono-elasticity: medical elasticity images de rived from ultra sound signals in mechanically vibrated targets. Acoust Imaging 1988;16:317–27.
4. Ophir J, Céspedes I, Ponnekanti H, Yazdi Y, Li X. Elastography: a quantitative method for imaging the elasticity of biological tissues. Ultrasonic Imaging 1991;13:111–34. [PubMed: 1858217]
5. Skovoroda AR, Emelianov SY, Lubinski MA, Sarvazyan AP, O'Donnell M. Theoretical analysis and verification of ultra sound displacement and strain imaging. IEEE Trans UFFC 1994;41:302–13.
6. Hall TJ, Zhu Y, Spalding CS. In vivo real-time free-hand palpation imaging. Ultrasound Med Biol 2003;29:427–35. [PubMed: 12706194]
7. Sarvazyan, AP.; Skovoroda, AR. The new approaches in ultrasonic visualization of cancers and their qualitative mechanical characterization for the differential diagnostics.. Abstract of the all-union conference “the actual problems of the cancer ultrasonic diagnostics”; Moscow. 1990;
8. Kim K, Weitzel WF, Rubin JM, Xie H, Chen X, O'Donnell M. Vascular intramural strain imaging using vessel pressure equalization. Ultrasound Med Biol 2004;30(6):761–71. [PubMed: 15219956]
9. Lerner RM, Huang SR, Parker KJ. Sono-elasticity images derived from ultrasound signals in mechanically vibrated tissues. Ultrasound Med Biol 1990;16:231–9. [PubMed: 1694603]
10. Ophir J, Céspedes I, Garra B, et al. Elastography: ultrasonic imaging of tissue strain and elastic modulus in vivo. Eur J Ultrasound 1996;3:49–70.
11. Geiman BJ, Bohs LN, Anderson ME, Breit SM, Trahey GE. A novel interpolation strategy for estimating subsample speckle motion. Phys Med Biol 2000;45:1541–52. [PubMed: 10870709]
12. Konofagou EE, Ophir J. A new method for estimation and imaging of lateral strains and Poisson's ratios in tissues. Ultrasound Med Biol 1998;24:1183–99. [PubMed: 9833588]

13. Insana MF, Hall TJ. 2-D companding for noise reduction in strain imaging. IEEE Trans UFFC 1998;45:179–91.
14. Lubinski MA, Emelianov SY, Raghavan KR, et al. Lateral displacement estimation using tissue incompressibility. IEEE Trans UFFC 1996;43:247–55.
15. Lubinski MA, Emelianov SY, O'Donnell M. Speckle tracking methods for ultrasonic elasticity imaging using short time correlation. IEEE Trans UFFC 1999;46:82–96.
16. Tristam M, Barbosa DC, Cosgrove DO, Bamber JC, Hill CR. Application of Fourier analysis to clinical study of patterns of tissue motion. Ultrasound Med Biol 1988;14:695–707. [PubMed: 3062864]
17. Yamakoshi Y, Sato J, Sato T. Ultrasonic imaging of internal vibration of soft tissue under forced vibration. IEEE Trans UFFC 1990;37:45–53.
18. O'Donnell M, Skovoroda AR, Shapo BM, Emelianov SY. Internal displacement and strain imaging using ultrasonic speckle tracking. IEEE Trans UFFC 1994;41(3):314–25.
19. Gao L, Parker KJ, Lerner RM, Levinson SF. Imaging of the elastic properties of tissue – a review. Ultrasound Med Biol 1996;22:959–77. [PubMed: 9004420]
20. Bilgen M, Insana MF. Deformation models and correlation analysis in elastography. J Acoust Soc Am 1996;99:3212–24. [PubMed: 8642127]
21. Shapo BM, Crowe JR, Skovoroda AR, Eberle MJ, Cohn NA, O'Donnell M. Displacement and strain imaging of coronary arteries with intraluminal ultrasound. IEEE Trans UFFC 1996;43:234–46.
22. de Korte CL, Pasterkamp G, van der Steen AFW, Woutman HA, Bom N. Characterization of plaque components with intravascular ultrasound elastography in human femoral and coronary arteries in vitro. Circulation 2000;102:617–23. [PubMed: 10931800]
23. Choi CD, Skovoroda AR, Emelianov SY, O'Donnell M. An integrated compliant balloon ultrasound catheter for intravascular strain imaging. IEEE Trans UFFC 2002;49(11):1552–60.
24. Rubin JM, Aglyamov SR, Wakefield TW, O'Donnell M, Emelianov SY. Clinical application of sonographic elasticity imaging for aging of deep venous thrombosis: preliminary findings. J Ultrasound Med 2003;22:443–8. [PubMed: 12751855]
25. Rubin JM, Xie H, Kim K, Weitzel WF, Emelianov SY, Aglyamov SR, et al. Sonographic elasticity imaging of acute and chronic DVT in humans. J Ultrasound Med 2006;25(9):1179–86. [PubMed: 16929019]
26. Garra BS, Céspedes EI, Ophir J, Spratt RS, Zuurbier RA, Magnant CM, et al. Elastography of breast lesions: initial clinical results. Radiology 1997;202:79–86. [PubMed: 8988195]
27. Hall TJ, Zhu Y, Spalding CS. In vivo real-time free-hand palpation imaging. Ultrasound Med Biol 2003;29:427–36. [PubMed: 12706194]
28. Lyshchik A, Higashi T, Asato R, Tanaka S, Ito J, Mai JJ, et al. Thyroid gland tumor diagnosis at US elastography. Radiology 2005:202–11. [PubMed: 16118150]
29. Lyshchik A, Higashi T, Asato R, Tanaka S, Ito J, Hiraoka M, et al. Cervical lymph node metastases: diagnosis at sonoelastography – initial experience. Radiology 2007;243:258–67. [PubMed: 17293571]
30. Cochlin DL, Ganatra RH, Griffiths DF. Elastography in the detection of prostatic cancer. Clin Radiol 2002;57(11):1014–20. [PubMed: 12409113]
31. Lorenz A, Sommerfield HJ, Garcia-Schurmann MG, Philippou S, Senge T, Ermert H. A new system for the acquisition of ultrasonic multi-compression strain images of human prostate in vivo. IEEE Trans UFFC 1999;46:1147–54.
32. Weitzel WF, Kim K, Rubin JM, Wiggins RC, Xie H, Chen X, et al. Feasibility of applying ultrasound strain imaging to detect renal transplant chronic allograft nephropathy. Kidney Int 2004;65(2):733–6. [PubMed: 14717949]
33. Weitzel WF, Kim K, Rubin JM, Xie H, Chen X, O'Donnell M. Renal advances in ultrasound elasticity imaging: measuring the compliance of arteries and kidneys in end-stage renal disease. Blood Purificat 2005;23:10–7.
34. Perk G, Tunick PA, Kronzon I. Non-Doppler two-dimensional strain imaging by echocardiography – from technical considerations to clinical applications. J Am Soc Echocard 2007;20:234–43.

35. Maurice RL, Fromageau J, Brusseau E, Finet G, Rioufol G, Cloutier G. On the potential of the Lagrangian estimator for endovascular ultrasound elastography: in vivo human coronary artery study. Ultrasound Med Biol 2007;33(8):1199–205. [PubMed: 17466446]
36. Ribbers H, Lopata R, Holewijn S, Pasterkamp G, Blankensteijn J, de Korte C. Non-invasive two-dimensional strain imaging of arteries: validation in phantoms and preliminary experience in carotid arteries in vivo. Ultrasound Med Biol 2007;33(4):530–40. [PubMed: 17280769]
37. Yang J, Webb AR, Pickerill SJ, Hageman G, Ameer GA. Synthesis and evaluation of poly(diol citrate) biodegradable elastomers. Biomaterials 2006;27(9):1889–98. [PubMed: 16290904]
38. Kang Y, Yang J, Khan S, Anissian L, Ameer GA. A new biodegradable polyester elastomer for cartilage tissue engineering. J Biomed Mater Res A 2006;77:331–9. [PubMed: 16404714]
39. Hollister SJ, Maddox RD, Taboas JM. Optimal design and fabrication of scaffolds to mimic tissue properties and satisfy biological constraints. Biomaterials 2002;23:4095–103. [PubMed: 12182311]
40. Hollister SJ. Porous scaffold design for tissue engineering. Nat Mater 2005;4:518–24. [PubMed: 16003400]
41. Hollister SJ, Lin CY. Computational design for tissue engineering scaffolds. Comp Meth Appl Mech Eng 2007;196:2991–8.
42. Bourne BC, van der Meulen MCH. Finite element models predict cancellous apparent modulus when tissue modulus is scaled from specimen CT-attenuation. J Biomech 2004;37(5):613–22. [PubMed: 15046990]
43. Erkamp RQ, Wiggins P, Skovoroda AR, Emelianov SY, O'Donnell M. Measuring the elastic modulus of small tissue samples. Ultrasonic Imaging 1998;20:17–28. [PubMed: 9664648]
44. Cohn NA, Kim BS, Erkamp RQ, Mooney DJ, Emelianov SY, O'Donnell M. High resolution elasticity imaging for tissue engineering. IEEE Trans UFFC 2000;47:956–66.
45. Chen X, Xie H, Erkamp R, Kim K, Jia C, Rubin JM, et al. 3-D correlation-based speckle tracking. Ultrasonic Imaging 2005;27:21–36. [PubMed: 16003924]
46. Oberai AA, Gokhale NH, Doyley MM, Bamber JC. Evaluation of the adjoint equation based algorithm for elasticity imaging. Phys Med Biol 2004;49:2955–74. [PubMed: 15285258]
47. Richards, MS.; Oberai, AA.; Barbone, PE.; Gokhale, NH. Three dimensional ultrasound image registration and shear modulus reconstruction.. 151st meeting of the acoustical society of America; 2006;

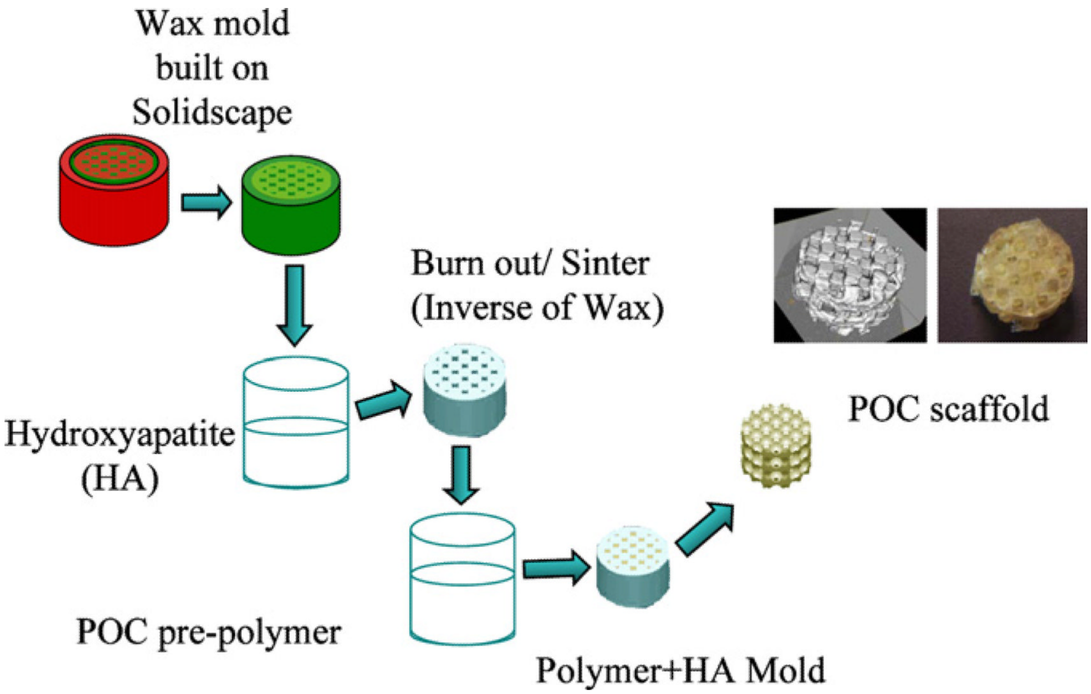

Fig. 1.

Scaffold fabrication process. HA molds (inverse of the wax molds) are fabricated using thermally curable HA slurry poured into wax molds built on Solidscape machine. The HA molds are then embedded within the pPOC. The pPOC/HA construct inside PTFE mold is post-polymerized at 80 °C for 4 days with vacuum in an oven. The HA + POC construct is removed from the PTFE mold and the HA mold from the construct is dissolved using RDO to obtain the final POC scaffold. The internal structure of the scaffold was examined using micro CT.

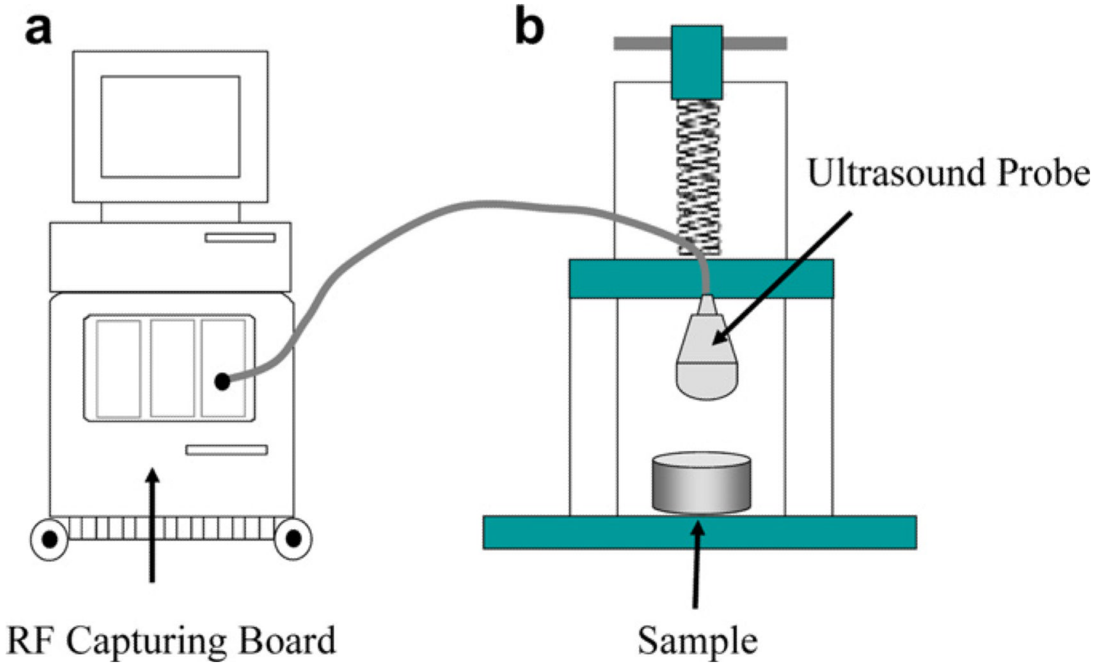

Fig. 2.

Experimental set-up. A commercial ultrasound scanner (iU22, Philips) with RF capturing board is used to collect ultrasound frames (a) while the sample (scaffold inside gel phantom or mouse) is deformed by an ultrasound probe connected to a laboratory built deformation device (b).

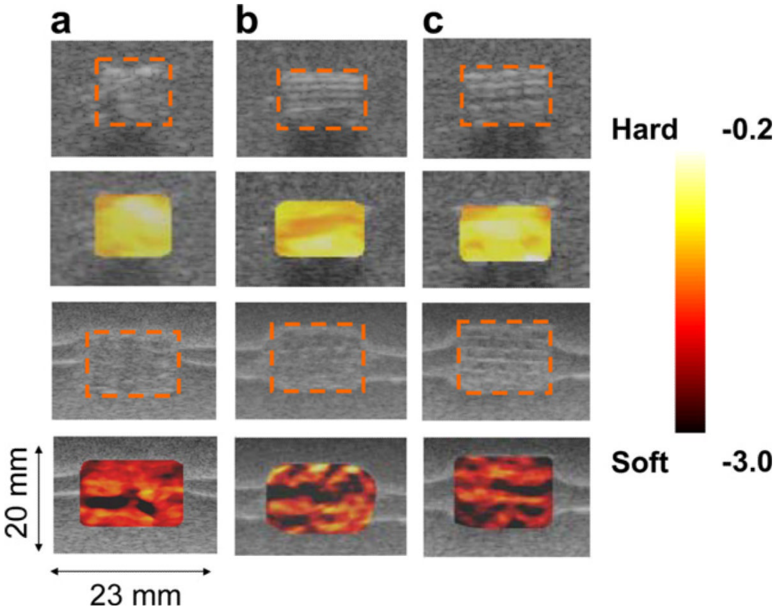

Fig. 3.

In vitro strain maps overlaid on top of the B-scan for the scaffold samples from the same batch before degradation (first two rows) and after (a) 41.6%, (b) 45.5% and (c) 42.0% degradation by weight (third and fourth rows). The dotted orange boxes represent the scaffolds. The average normalized strain generated inside of the scaffold after the degradation (–2.97 ± 0.74) of about 43% by weight was much higher than before the degradation (–0.43 ± 0.03) of the scaffolds. The coefficient of variation (COV = standard deviation/mean) after the degradation (25%) was much higher than before the degradation (7%). The inhomogeneity of the strain map also reflects the possible heterogeneous distribution of the internal structural degradation. In the lower two columns, the horizontal bright lines around the scaffolds are due to the ultrasound reflection between the layers formed during gel phantom fabrication. These do not affect the mechanical property of the phantom.

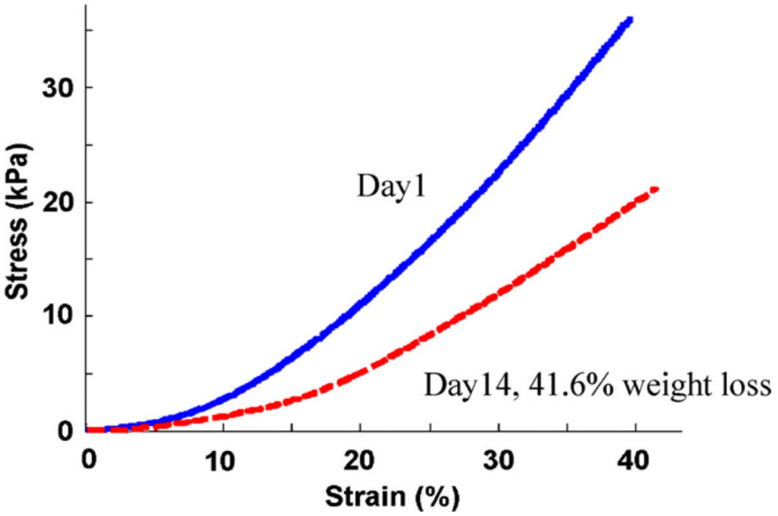

Fig. 4.

Direct mechanical measurements for an in vitro sample (in vitro sample 1 in Table 1). The slope of the stress–strain curve for the scaffold before degradation (solid blue) is stiffer than the 41.6% weight degraded scaffold (dashed red). The reconstructed elastic moduli were 89.1 and 38.7 kPa before and after the degradation, respectively. (For interpretation of the references to colour in this figure legend, the reader is referred to the web version of this article.)

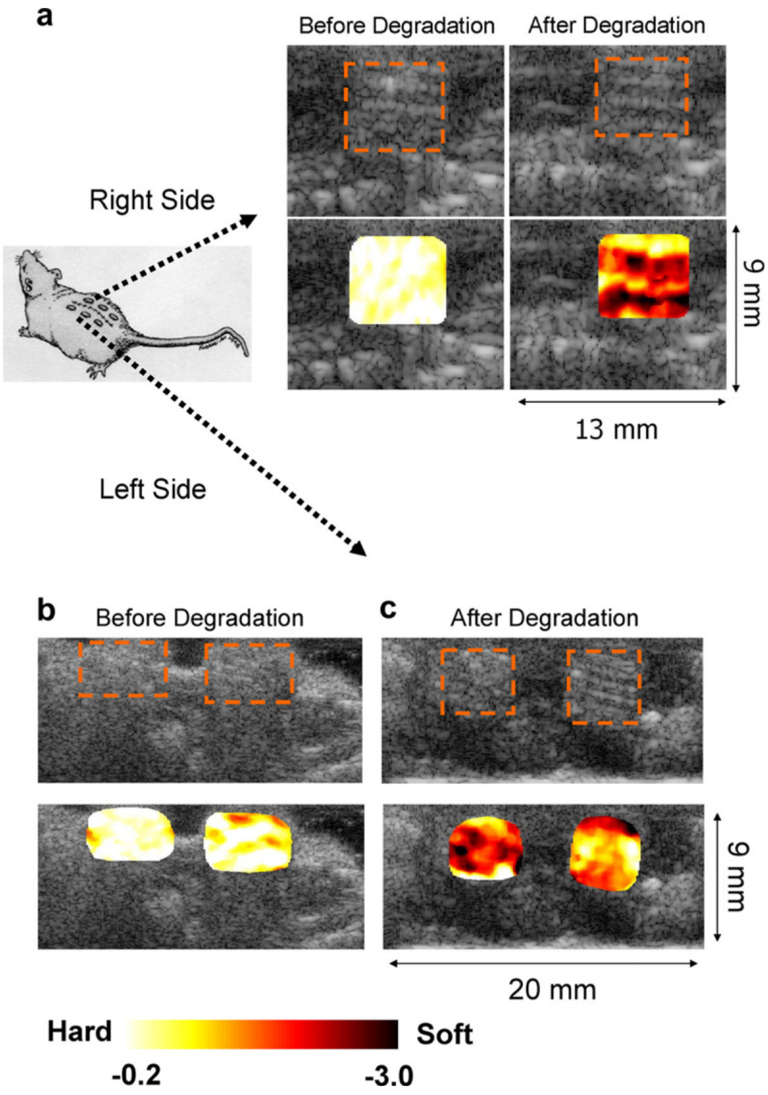

Fig. 5.

In vivo strain maps overlaid on top of B-scan for the scaffold samples implanted underneath of the skin on the right (a) and left hand sides (b, c) of the mouse back before and after degradation by weight ((a), 13.6%, left side of (c), 26.5%, and right side of (c) 28.6%). Overall, the scaffolds after the degradation of about 23% by weight generated much higher strains (–1.40 ± 0.24) than those before the degradation (–0.21 ± 0.01). The COV before the degradation (4.8%) was increased to 17% after the degradation. The inhomogeneity of the strain map also reflects the possible heterogeneous distribution of the structural degradation.

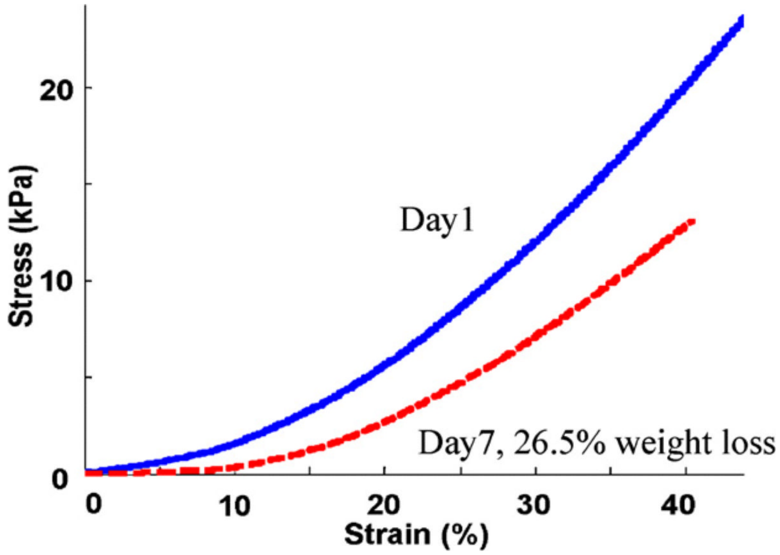

Fig. 6.

Direct mechanical measurements for an in vivo sample (in vivo sample 2 in Table 1). The slope of the stress–strain curve for the scaffold before degradation (solid blue) is stiffer than after 26.5% weight degradation (dashed red). The reconstructed elastic moduli are 56.4 and 38.1 kPa before and after the degradation, respectively. (For interpretation of the references to colour in this figure legend, the reader is referred to the web version of this article.)

Table 1

Weight loss, strain and elastic modulus for in vitro and in vivo

Study	Samples		W (g)	Normalized strain	E (kPa)	Correlation (r^2)
In vitro	1	Day 1	0.183	–0.37 ± 0.03	89.1	0.9886
		Day 14	0.107	–2.5 ± 1.0	38.7	0.9549
	2	Day 1	0.152	–0.51 ± 0.07	74.9	0.9862
		Day 14	0.083	–2.9 ± 1.5	42.6	0.9715
	3	Day 1	0.126	–0.4 ± 0.03	58.2	0.9944
		Day 14	0.072	–3.5 ± 1.3	31.7	0.9552
In vivo	1	Day 1	0.125	–0.18 ± 0.01	55.8	0.9936
		Day 7	0.108	–1.5 ± 0.5	41.3	0.9974
	2	Day 1	0.121	–0.21 ± 0.01	56.4	0.9937
		Day 7	0.089	–1.7 ± 0.4	38.1	0.9971
	3	Day 1	0.126	–0.25 ± 0.02	53.8	0.9831
		Day 7	0.090	–1.0 ± 0.3	33.5	0.9696

r^2 represents the coefficient of determination for the curve fitting of the stress–strain relationship.